VTI Migration velocity analysis using RTM

Yunyue (Elita) Li, Stanford University; Peng Shen, Shell IEP; Colin Perkins, Shell IEP*

ABSTRACT

In this paper, we use VTI two-way propagation engine (RTM) to perform wave-equation migration velocity analysis. Using RTM, we have a chance to characterize the wavefields propagating in large angles and image steeply dipping reflectors. By including VTI Thomson parameters, we can better describe the property of the subsurface. We first derive the MVA gradient when using first-order VTI two-way wave-equation. Then, we test our method on a synthetic VTI Marmousi model. The inversion results show that our method can resolve a better velocity model and a better focused subsurface image.

INTRODUCTION

Velocity model building has been one of the most challenging problems in the exploration industry. Wave-Equation Migration Velocity Analysis (WEMVA) has been widely studied for velocity building and can be implemented either in the data space (Tarantola, 1984; Woodward, 1992) or in the image space (Sava and Biondi, 2004a,b; Shen, 2004; Shen and Symes, 2008; Guerra et al., 2009). Several advantages drive us to use the image-space WEMVA instead of data-space WEMVA (known as Full-Waveform Inversion): first, migrated image is often much cleaner than the recorded wavefields; second, the objective function is directly related to the final image; third, image-space WEMVA doesn't require such close initial solution as FWI does to avoid the cycle-skipping problem. In fact, the optimized output of the image-space WEMVA can be used as the input for FWI (Li and Biondi, 2011).

On the other hand, since first reported in exploration seismology in the 1930s (McCollum and Snell, 1932), anisotropy has become increasingly important in seismic imaging and exploration. The increasing offset and azimuth in data acquisition has heightened the need for anisotropic imaging and model building. Until now, the transverse isotropic (TI) model has been the most commonly used in seismic imaging and considered as a better description of the subsurface. Li and Biondi (2011) extend the WEMVA framework to VTI media using one-way wave-equation. However, one-way wave-equation cannot accurately describe the wave propagation in large angles, where anisotropy has larger effects. There has been extensive studies on anisotropic RTM with increasingly complex subsurface models (Fletcher et al., 2009; Zhang and Zhang, 2009), while reliable anisotropic model building techniques are still in need.

Therefore, we propose an image-space WEMVA method using VTI two-way wave-equation as propagation engine, and evaluate the flatness of the reverse time migration (RTM) images in the angle domain. In this paper, we first derive the gradient of the DSO objective function with respect to velocity and ϵ using Lagrangian augmented functional. To resolve the ambiguity between velocity and ϵ and make sure our model honor the geology, we use a preconditioning inversion scheme. Finally, we test the proposed method on a synthetic VTI Marmousi model.

FIRST-ORDER TWO-WAY VTI WAVE-EQUATION

First-order two-way VTI wave-equation can be derived from Hooke's law and Newton's law using Thomsen anisotropy parameters and setting $c_s = 0$ (Duveneck et al., 2008). The first-order system reads as follows:

$$\begin{aligned}
\rho\partial_t v_x &= -\partial_x p_H \\
\rho\partial_t v_y &= -\partial_y p_H \\
\rho\partial_t v_z &= -\partial_z p_V \\
\frac{1}{\rho c^2}\partial_t p_V &= -\sqrt{(1+2\delta)}(\partial_x v_x + \partial_y v_y) - \partial_z v_z + f_V \\
\frac{1}{\rho c^2}\partial_t p_H &= -(1+2\epsilon)(\partial_x v_x + \partial_y v_y) - \sqrt{(1+2\delta)}\partial_z v_z + f_H
\end{aligned} \tag{1}$$

where (v_x, v_y, v_z) is particle velocity vector, p_V and p_H are pressure in the vertical and horizontal direction, respectively. Source term f_V and f_H are defined as:

$$f_V(t) = f_H(t) = \int_{-\infty}^{\tau} w(\tau)d\tau. \tag{2}$$

It is straightforward to see when $\rho = 1$, $\epsilon = 0$ and $\delta = 0$, the first order system (1) is equivalent to the familiar isotropic acoustic second-order wave-equation:

$$\frac{1}{c^2}\partial_t^2 p - \nabla p = w. \tag{3}$$

For simplicity, we can rewrite system (1) in a matrix-vector notation:

$$\mathbf{L}(c)\mathbf{p} = \mathbf{f}, \tag{4}$$

where $\mathbf{p} = (v_x,\ v_y,\ v_z,\ p_V,\ p_H)^T$, $\mathbf{f} = (0,\ 0,\ 0,\ f_V,\ f_H)^T$, and

$$\mathbf{L} = \begin{vmatrix}
\partial_t & 0 & 0 & 0 & \partial_x \\
0 & \partial_t & 0 & 0 & \partial_y \\
0 & 0 & \partial_t & \partial_z & 0 \\
\sqrt{1+2\delta}\partial_x & \sqrt{1+2\delta}\partial_y & \partial_z & \frac{1}{c^2}\partial_t & 0 \\
(1+2\epsilon)\partial_x & (1+2\epsilon)\partial_y & \sqrt{1+2\delta}\partial_z & 0 & \frac{1}{c^2}\partial_t
\end{vmatrix}. \tag{5}$$

VTI REVERSE-TIME MIGRATION IMAGING CONDITION

Traditionally, subsurface image is often considered as the first gradient of an FWI objective function with respect to velocity. In this paper, we are going to derive the VTI reverse-time migration imaging condition according to the same criteria.

Define FWI objective function is

$$J_{\mathrm{W}} = \frac{1}{2}\langle d - d_{\mathrm{est}}, d - d_{\mathrm{est}}\rangle, \tag{6}$$

where d_{est} is the data estimated from the current model, which is sampled from wavefield $\mathbf{p}$ and d is the recorded data.

For the first iteration, $d_{\mathrm{est}} = 0$. Therefore the first gradient in velocity is:

$$\begin{aligned} \nabla_c J_{\mathrm{W}} &= \left(\frac{\partial p}{\partial c}\right)^* d \\ &= (-\mathbf{L}^{-1}\frac{\partial \mathbf{L}}{\partial c}\mathbf{L}^{-1} f)^* d. \end{aligned} \tag{7}$$

Now we introduce the receiver vector field $\mathbf{q} = (u_x,\ u_y,\ u_z,\ q_V,\ q_H)^T$, which is the solution of the following equation:

$$\mathbf{L}^*(c)\mathbf{q} = \mathbf{f}\ '. \tag{8}$$

The equivalent source term in equation (8) is defined as $\mathbf{f}\ ' = (0,\ 0,\ 0,\ f'_V,\ f'_H)^T$, where $f'_V = f'_H = d$.

From equation (5), we have

$$\frac{\partial \mathbf{L}}{\partial c} = \begin{vmatrix} 0 & 0 & 0 & 0 & 0 \\ 0 & 0 & 0 & 0 & 0 \\ 0 & 0 & 0 & 0 & 0 \\ 0 & 0 & 0 & -\frac{2}{c^3}\partial_t & 0 \\ 0 & 0 & 0 & 0 & -\frac{2}{c^3}\partial_t \end{vmatrix}, \tag{9}$$

If we plug equation (8), (9) into equation (7), and ignore the velocity dependency, we arrive at the imaging condition as follows:

$$\begin{aligned} I &= \mathbf{p}^*\mathbf{M}^*\mathbf{q}, \\ &= (\mathbf{M}\mathbf{p})^*\mathbf{q}, \end{aligned} \tag{10}$$

where

$$\mathbf{M} = \begin{vmatrix} 0 & 0 & 0 & 0 & 0 \\ 0 & 0 & 0 & 0 & 0 \\ 0 & 0 & 0 & 0 & 0 \\ 0 & 0 & 0 & \frac{1}{2}\partial_t & 0 \\ 0 & 0 & 0 & 0 & \frac{1}{2}\partial_t \end{vmatrix}. \tag{11}$$

The explicit form of this imaging condition for acoustic RTM is:

$$I = \int_0^{t_{max}} \frac{1}{2} \left((\partial t p_H) q_H + (\partial t p_V) q_V \right) dt. \tag{12}$$

When $p_H = p_V$, equation (12) reduces to the isotropic cross-correlation imaging condition (Claerbout, 1987). For the propose of velocity analysis, we often work with extended images and generalized imaging conditions. Similarly, we define our subsurface-offset domain common image gathers (SODCIGs) $\mathbf{I}$ as a column vector:

$$\mathbf{I} = [I_{-\mathbf{h}_{\max}}, I_{-\mathbf{h}_{\max}+\Delta\mathbf{h}}, \cdots, I_{\mathbf{0}}, \cdots, I_{\mathbf{h}_{\max}-\Delta\mathbf{h}}, I_{\mathbf{h}_{\max}}]^*, \tag{13}$$

where $\mathbf{h}$ is the half-subsurface offset, which ranges from $-\mathbf{h}_{\max}$ to $\mathbf{h}_{\max}$ with an increment of $\Delta\mathbf{h}$. For each element $I_{\mathbf{h}}$, the extended imaging condition is (Sava and Formel, 2006):

$$I_{\mathbf{h}} = (\mathbf{S}_{+\mathbf{h}}\mathbf{p})^* \mathbf{M}^* (\mathbf{S}_{-\mathbf{h}}\mathbf{q}), \tag{14}$$

where $\mathbf{S}_{+\mathbf{h}}$ is a shifting operator which shifts the wavefield by an amount of $+\mathbf{h}$ in the $\mathbf{x}$ direction. Notice the relationship of $(\mathbf{S}_{+\mathbf{h}})^* = \mathbf{S}_{-\mathbf{h}}$.

MIGRATION VELOCITY ANALYSIS GRADIENTS

In this section, we derive the MVA gradients of objective function (15) by two different approaches: adjoint method from the perturbation theory and Lagrangian augmented function.

WEMVA is a non-linear inversion process that aims to find the background velocity model that minimizes the residual field $\Delta\mathbf{I}$ in the image space. Without losing any generality, we define our objective function by Differential Semblance optimization (DSO) (Shen and Symes, 2008) in the subsurface offset domain:

$$J = \frac{1}{2} \sum_{\mathbf{h}} \langle \mathbf{h} I_{\mathbf{h}}, \mathbf{h} I_{\mathbf{h}} \rangle. \tag{15}$$

Although we don't use this DSO objective function in the example, the derivation follows the same logic and readers can easily substitude their desired image-space objective function into the derivation.

Adjoint method from the perturbation theory

A perturbation, δc, of the velocity model c, induces a perturbation $\delta\mathbf{p}$ in the source wavefield vector $\mathbf{p}$, a perturbation $\delta\mathbf{q}$ in the receiver wavefield vector $\mathbf{q}$, a perturbation $\delta\mathbf{I}$ in the extended image cube $\mathbf{I}$, and hence a perturbation δJ in the objective function J. To the first order and using chain rule, δJ and δc have following relationship:

$$\delta J = \sum_{\mathbf{h}} \frac{\partial J}{\partial I_{\mathbf{h}}} \frac{\partial I_{\mathbf{h}}}{\partial \mathbf{p}} \frac{\partial \mathbf{p}}{\partial c} \delta c + \sum_{\mathbf{h}} \frac{\partial J}{\partial I_{\mathbf{h}}} \frac{\partial I_{\mathbf{h}}}{\partial \mathbf{q}} \frac{\partial \mathbf{q}}{\partial c} \delta c. \tag{16}$$

Now we can define the gradient by the back-projection of a unit perturbation in the objective function:

$$\begin{aligned}\nabla_c J &= \sum_{\mathbf{h}} \left(\frac{\partial J}{\partial I_{\mathbf{h}}}\frac{\partial I_{\mathbf{h}}}{\partial \mathbf{p}}\frac{\partial \mathbf{p}}{\partial c}\right)^* + \sum_{\mathbf{h}} \left(\frac{\partial J}{\partial I_{\mathbf{h}}}\frac{\partial I_{\mathbf{h}}}{\partial \mathbf{q}}\frac{\partial \mathbf{q}}{\partial c}\right)^* \\ &= (\nabla_c J)_1 + (\nabla_c J)_2 \,. \end{aligned} \tag{17}$$

Let's analyze the first term in equation (17) in detail, and the second term follows the same reasoning.

$$\begin{aligned}(\nabla_c J)_1 &= \sum_{\mathbf{h}} \left(\frac{\partial J}{\partial I_{\mathbf{h}}}\frac{\partial I_{\mathbf{h}}}{\partial \mathbf{p}}\frac{\partial \mathbf{p}}{\partial c}\right)^* \\ &= \sum_{\mathbf{h}} \left(\frac{\partial \mathbf{p}}{\partial c}\right)^* \left(\frac{\partial I_{\mathbf{h}}}{\partial \mathbf{p}}\right)^* \left(\frac{\partial J}{\partial I_{\mathbf{h}}}\right)^* \\ &= \sum_{\mathbf{h}} \mathbf{p}^* \left(-\frac{\partial \mathbf{L}}{\partial c}\right)^* \mathbf{L}^{-*} \left(\frac{\partial I_{\mathbf{h}}}{\partial \mathbf{p}}\right)^* \left(\frac{\partial J}{\partial I_{\mathbf{h}}}\right)^* \\ &= \mathbf{p}^* \left(-\frac{\partial \mathbf{L}}{\partial c}\right)^* \mathbf{L}^{-*} \sum_{\mathbf{h}} \left(\frac{\partial I_{\mathbf{h}}}{\partial \mathbf{p}}\right)^* \left(\frac{\partial J}{\partial I_{\mathbf{h}}}\right)^* \end{aligned} \tag{18}$$

where

$$\left(\frac{\partial J}{\partial I_{\mathbf{h}}}\right)^* = \mathbf{h}^* \mathbf{h} I_{\mathbf{h}}, \tag{19}$$

and

$$\begin{aligned}\left(\frac{\partial I_{\mathbf{h}}}{\partial \mathbf{p}}\right)^* &= (\mathbf{S}_{+\mathbf{h}})^* \mathbf{M}^* (\mathbf{S}_{-\mathbf{h}} \mathbf{q}) \\ &= \mathbf{S}_{-\mathbf{h}} \mathbf{M}^* (\mathbf{S}_{-\mathbf{h}} \mathbf{q}). \end{aligned} \tag{20}$$

Plugging equation (19) and (20) into equation (18), we can rewrite equation (18) explicitly as follows:

$$\left(\frac{\partial J}{\partial c}\right)_1 = \mathbf{p}^* \left(-\frac{\partial \mathbf{L}}{\partial c}\right)^* \mathbf{L}^{-*} \sum_{\mathbf{h}} \mathbf{S}_{-\mathbf{h}} \mathbf{M}^* (\mathbf{S}_{-\mathbf{h}} \mathbf{q}) \mathbf{h}^2 I_{\mathbf{h}} \tag{21}$$

Similarly, we can obtain the explicit form for the second term in equation (17):

$$\left(\frac{\partial J}{\partial c}\right)_2 = \mathbf{q}^* \left(-\frac{\partial \mathbf{L}}{\partial c}\right) \mathbf{L}^{-1} \sum_{\mathbf{h}} \mathbf{S}_{+\mathbf{h}} \mathbf{M} (\mathbf{S}_{+\mathbf{h}} \mathbf{p}) \mathbf{h}^2 I_{\mathbf{h}} \tag{22}$$

Substituting equation (21) and equation (22) with the corresponding term in equation (17), we now have derived the explicit form for the DSO gradient.

Lagrangian augmented functional method

We are now going to use the recipe with the augmented functional that Plessix (2006) provides to derive the image-space DSO gradient. First, let us form the Lagrangian augmented functional, $\mathcal{L}$:

$$\begin{aligned}\mathcal{L}(\mathbf{p},\mathbf{q},I_{\mathbf{h}},\lambda,\mu,\gamma_{\mathbf{h}},c) = & \qquad (23)\\ & \sum_{\mathbf{h}}\frac{1}{2}\langle \mathbf{h}\ I_{\mathbf{h}},\ \mathbf{h}\ I_{\mathbf{h}}\rangle \\ & +\langle\lambda,\ \mathbf{f}-\mathbf{L}(\mathbf{c})\mathbf{p}\rangle \\ & +\langle\mu,\ \mathbf{f}\ '-\mathbf{L}^*(\mathbf{c})\mathbf{q}\rangle \\ & +\sum_{\mathbf{h}}\langle\gamma_{\mathbf{h}},\ (\mathbf{S}_{+\mathbf{h}}\mathbf{p})^*\mathbf{M}^*(\mathbf{S}_{-\mathbf{h}}\mathbf{q})-I_{\mathbf{h}}\rangle \qquad (24)\end{aligned}$$

Then the adjoint state equations are obtained by taking the derivative of $\mathcal{L}$ with respect to state variables $\mathbf{p}$, $\mathbf{q}$ and $I_{\mathbf{h}}$:

$$\frac{\partial\mathcal{L}}{\partial\mathbf{p}} = -\mathbf{L}^*(c)\lambda+\sum_{\mathbf{h}}(\mathbf{S}_{+\mathbf{h}})^*\mathbf{M}^*(\mathbf{S}_{-\mathbf{h}}\mathbf{q})\gamma_{\mathbf{h}}=\mathbf{0}, \qquad (25)$$

$$\frac{\partial\mathcal{L}}{\partial\mathbf{q}} = -\mathbf{L}(c)\mu+\sum_{\mathbf{h}}(\mathbf{S}_{-\mathbf{h}})^*\mathbf{M}(\mathbf{S}_{+\mathbf{h}}\mathbf{p})\gamma_{\mathbf{h}}=\mathbf{0}, \qquad (26)$$

$$\frac{\partial\mathcal{L}}{\partial I_{\mathbf{h}}} = -\gamma_{\mathbf{h}}+\mathbf{h}^2 I_{\mathbf{h}}=0,\forall\ \mathbf{h}. \qquad (27)$$

Equation (25), (26), (27) are the adjoint-state equations. Variable $\lambda=(\lambda_x,\lambda_y,\lambda_z,\lambda_V,\lambda_H)^T$ and $\mu=(\mu_x,\mu_y,\mu_z,\mu_V,\mu_H)^T$ are the ajoint-state fields and the solution of the adjoint-state equations.

Now the gradient of the objective function (15) with respect to velocity is:

$$\begin{aligned}\nabla_c J &= \left\langle\lambda,\ -\frac{\partial\mathbf{L}}{\partial\mathbf{c}}\mathbf{p}\right\rangle+\left\langle\mu,\ -\frac{\partial\mathbf{L}^*}{\partial\mathbf{c}}\mathbf{q}\right\rangle \\ &= \left(-\frac{\partial\mathbf{L}}{\partial c}\mathbf{p}\right)^*\lambda+\left(-\frac{\partial\mathbf{L}^*}{\partial\mathbf{c}}\mathbf{q}\right)^*\mu, \qquad (28)\end{aligned}$$

If we combine equation (25), (26), (27) with equation (28), we will arrive at the same solution as the previous section.

Extend to update anisotropic parameters

The extension from isotropic model updates to anisotropic updates is straightfoward. Built on the derivations in the last section, we can easily get the gradients for

anisotropic parameters ϵ and δ as follows:

$$\begin{aligned}\nabla_\epsilon J &= \left\langle \lambda, \; -\frac{\partial \mathbf{L}}{\partial \epsilon}\mathbf{p} \right\rangle + \left\langle \mu, \; -\frac{\partial \mathbf{L}^*}{\partial \epsilon}\mathbf{q} \right\rangle \\ &= \left(-\frac{\partial \mathbf{L}}{\partial \epsilon}\mathbf{p}\right)^* \lambda + \mathbf{q}^* \left(-\frac{\partial \mathbf{L}}{\partial \epsilon}\right) \mu, \end{aligned} \tag{29}$$

$$\begin{aligned}\nabla_\delta J &= \left\langle \lambda, \; -\frac{\partial \mathbf{L}}{\partial \delta}\mathbf{p} \right\rangle + \left\langle \mu, \; -\frac{\partial \mathbf{L}^*}{\partial \delta}\mathbf{q} \right\rangle \\ &= \left(-\frac{\partial \mathbf{L}}{\partial \delta}\mathbf{p}\right)^* \lambda + \mathbf{q}^* \left(-\frac{\partial \mathbf{L}}{\partial \delta}\right) \mu, \end{aligned} \tag{30}$$

where

$$\frac{\partial \mathbf{L}}{\partial \epsilon} = \begin{vmatrix} 0 & 0 & 0 & 0 & 0 \\ 0 & 0 & 0 & 0 & 0 \\ 0 & 0 & 0 & 0 & 0 \\ 0 & 0 & 0 & 0 & 0 \\ 2\partial_x & 2\partial_y & 0 & 0 & 0 \end{vmatrix}, \tag{31}$$

$$\frac{\partial \mathbf{L}}{\partial \delta} = \begin{vmatrix} 0 & 0 & 0 & 0 & 0 \\ 0 & 0 & 0 & 0 & 0 \\ 0 & 0 & 0 & 0 & 0 \\ \frac{\partial_x}{\sqrt{1+2\delta}} & \frac{\partial_y}{\sqrt{1+2\delta}} & 0 & 0 & 0 \\ 0 & 0 & \frac{\partial_z}{\sqrt{1+2\delta}} & 0 & 0 \end{vmatrix}. \tag{32}$$

It is well-known that δ is the worst constrained parameter by surface seismic. Therefore, in our study, we assume the δ is obtained from well-logs or seismic-well ties and only invert for velocity and ϵ.

Physical interpretation and implementation of the DSO gradient

In this subsection, we will interpret each term in the DSO gradient formulation, and provide the readers with some hints of implementation. We find it is easier to interpret using the Lagrangian formulation, and readers can clearly relate the corresponding terms with the adjoint formulation. We will only discuss the physical meaning and the implementation for the first term in the gradient (Equation 28 and 25). Then similar reasoning can be argued using reciprocity.

First, for each image slice in the subsurface-offset domain $I_{\mathbf{h}}$ we compute a weighted image using equation (27). Then we move on to equation (25). We can rearrange the independent and commutable operators as follows:

$$\mathbf{L}^*(c)\lambda = \sum_{\mathbf{h}} \mathbf{S}_{-\mathbf{h}} \left(\mathbf{S}_{-\mathbf{h}} \mathbf{M}^* \mathbf{q}\right) \gamma_{\mathbf{h}}. \tag{33}$$

Operator $\mathbf{M}^*$ corresponds to differentiating q_V and q_H once reversely in time and zeroing out u_x, u_y, u_z fields. Notice the direction of propagation and differentiation of wavefield $\mathbf{q}$ are the same. Therefore, we can compute the time derivative during the same process as the propagation. Then we shift the reverse-time derivative $\mathbf{q}$ by $-\mathbf{h}$ in $\mathbf{x}$, and multiply it with the weighted image $\gamma_{\mathbf{h}}$. This product is shifted again by $-\mathbf{h}$. Finally, we sum over all the contributions from all the subsurface offset image slices to get an effective source term $\mathbf{f}_p$. Next, we solve equation (33) for λ backward in time using $\mathbf{f}_p$ as the source.

At the same time, in equation (28) $-\frac{\partial \mathbf{L}}{\partial c}$ is a sparse matrix with non-zero elements only for p_V and p_H. We can therefore write everything out explicitly:

$$(\nabla_c J)_1 = \int_0^{t_{max}} \frac{2}{c^3} \left[(\partial_t p_H)\lambda_H + (\partial_t p_V)\lambda_V \right] dt. \tag{34}$$

The explicit form for the complete gradients are:

$$\begin{aligned} \nabla_c J &= \int_0^{t_{max}} \frac{2}{c^3} \left[(\partial_t p_H)\lambda_H + (\partial_t p_V)\lambda_V \right] dt \\ &+ \int_0^{t_{max}} \frac{2}{c^3} \left[(\partial_t q_H)\mu_H + (\partial_t q_V)\mu_V \right] dt. \end{aligned} \tag{35}$$

$$\begin{aligned} \nabla_\epsilon J &= -\int_0^{t_{max}} [(\partial_x v_x)\lambda_H + (\partial_y v_y)\lambda_H] dt \\ &+ \int_0^{t_{max}} [(\partial_x q_H)\mu_x + (\partial_y q_H)\mu_y] dt. \end{aligned} \tag{36}$$

Preconditioning of the DSO gradient

Velocity model building is a highly underdetermined and nonlinear problem. Therefore, prior knowledge of the subsurface is needed to define a plausible subsurface model. In the formulation of Tarantola (1984), prior information is included as the covariance and the mean of the model. In this study, we assume the initial model we use is the mean, and the covariance of the model has two independent components: spatial covariance and colocated cross-parameter covariance (Li et al., 2011). In practice, instead of regularizing the inversion using Tarantola (1984), we use a preconditioning scheme (Claerbout, 2009): smoothing filtering to approximate square-root of the spatial covariance, standard deviation matrix to approximate square-root of the cross-parameter covariance.

Mathematically, the preconditioned model perturbation $d\mathbf{n}$ of the subsurface is defined as follows:

$$d\mathbf{m} = \mathbf{B}\mathbf{\Sigma} d\mathbf{n}, \tag{37}$$

where $\mathbf{m} = [c\ \epsilon]^T$. The smoothing operator $\mathbf{B}$ is a diagnal matrix:

$$\mathbf{B} = \begin{vmatrix} \mathbf{B}_c & 0 \\ 0 & \mathbf{B}_\epsilon \end{vmatrix}. \tag{38}$$

with different smoothing operator for velocity and ϵ according to the geological information in the study area. The standard deviation matrix Σ:

$$\mathbf{\Sigma} = \begin{vmatrix} \sigma_{cc} & \sigma_{c\epsilon} \\ \sigma_{\epsilon c} & \sigma_{\epsilon\epsilon} \end{vmatrix}. \tag{39}$$

can be obtained by rock physics modeling and/or lab measurements (Bachrach et al., 2011; Li et al., 2011).

We call $\mathbf{n}$ the preconditioning variable, and it relates to the original model $\mathbf{m}$ by:

$$\mathbf{m} = \mathbf{B\Sigma n} + (\mathbf{m}_0 - \mathbf{B\Sigma n}_0), \tag{40}$$

where $\mathbf{n}_0$ and $\mathbf{m}_0$ are the initial models in preconditioned space and physical space, respectively. Now, the gradient of the objective function 15 with respect to this preconditioning variable n is:

$$\begin{aligned} \nabla_{\mathbf{n}} J &= (\frac{\partial \mathbf{m}}{\partial \mathbf{n}})^* \nabla_{\mathbf{m}} J \\ &= \mathbf{\Sigma}^* \mathbf{B}^* \nabla_{\mathbf{m}} J, \end{aligned} \tag{41}$$

where $\nabla_{\mathbf{m}} J = [\nabla_c J \ \nabla_\epsilon J]^T$.

In a steepest decent inversion framework, the initial preconditioning model $\mathbf{n}_0$is obtained by minimizing the following objective function:

$$J_{\text{init}} = \frac{1}{2} \langle \mathbf{m}_0 - \mathbf{B\Sigma n}_0, \mathbf{m}_0 - \mathbf{B\Sigma n}_0 \rangle \tag{42}$$

For the i_{th} iteration:

$$\mathbf{n}_{i+1} = \mathbf{n}_i + \alpha_i \nabla_{\mathbf{n}} J, \tag{43}$$

$$\begin{aligned} \mathbf{m}_{i+1} &= \mathbf{B\Sigma n}_{i+1} \\ &= \mathbf{B\Sigma n}_i + \alpha_i \mathbf{B\Sigma} \nabla_{\mathbf{n}} J \\ &= \mathbf{m}_i + \alpha_i \mathbf{B\Sigma\Sigma}^* \mathbf{B}^* \nabla_{\mathbf{m}} J. \end{aligned} \tag{44}$$

Equation 44 suggests an interesting note that in the context of nonlinear inversion, left multiplying the gradient with a (semi)positive-definite matrix is equivalent to preconditioning with the square-root of the matrix; thus, the resulting direction is still a decent direction (Claerbout, 2009).

NUMERICAL TEST

In this section, we present the tests of our method on a synthetic VTI Marmousi model. We perform the tests in three steps: Objective function test, single parameter inversion, and joint inversion for two parameters.

Objective function test

We test our method on a VTI Marmousi model. First, synthetic born data is generated using the models in figure 1 and figure 2. The maximum offset is 3 km. Next, we perturb the ϵ model (Figure 2(a)) by a very smooth $\delta\epsilon$ field as shown in Figure 3. We change the perturbation from -50% to 50% of the true ϵ model, and calculate the corresponding objective function respectively.

Ideally, we'd like to choose an objective function that reaches local minimum at the correct model and is quadratic around the correct model so that a gradient-based inversion scheme is guaranteed to converge. Based on the results, we choose an angle domain objective function instead of the DSO objective function (Equation 15):

$$J = \frac{1}{2}\langle \mathbf{DRI}, \mathbf{DRI} \rangle, \tag{45}$$

where $\mathbf{R}$ is the Radon transform operator, and $\mathbf{D}$ is the derivative operator along the ray-parameter axis.

As shown in Figure 4, the angle domain objective function minimizes at the correct epsilon model, and has a semi-quadratic shape with respect to the model perturbation. Therefore, this objective function is a good measure of the error in the anisotropic model. Notice that the tilting effect toward negative ϵ perturbation is caused by the limited acquisition geometry. This effect is negligible for velocity perturbation because velocity has a first-order effect on the flatness of the angle gather, while ϵ's effect is second-order. We can increase the acquisition offset to mitigate this tilting effect and help the inversion.

Single parameter inversion

In this subsection, we invert for anisotropic parameter ϵ alone. In this test, we model the synthetic data using very smooth ϵ (Figure 5(a)) and δ (Figure 5(b)) models as suggested by many field applications. To better constrain the inversion for ϵ, we also increase the maximum offset in the acquisition to 6 km.

Compared with the true ϵ model, our initial ϵ model (Figure 6(a)) has about negative 50% perturbation in the shallower part. Because a perfect velocity model is used in this case, the moveout at large angles is so small that it is almost negligible to human eyes (Figure 6(b)). However, our inversion scheme is very sensitive to the residual moveout and successfully updates the ϵ model to the correct direction. Figure 7 shows the inverted ϵ model and the corresponding angle domain common image gathers after 40 iterations. Comparing with the initial angle gathers (Figure 6(b)), we can see that the slightly curving events at large angles are flattened and the inverted ϵ model is closer to the true one.

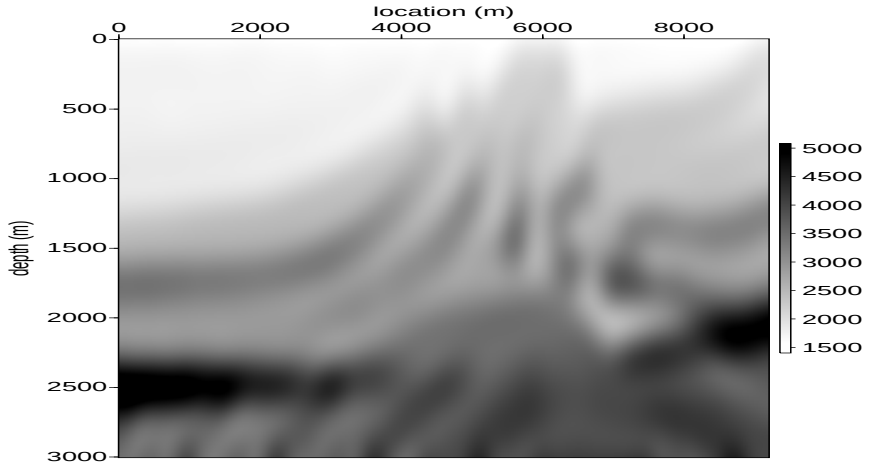

(a)

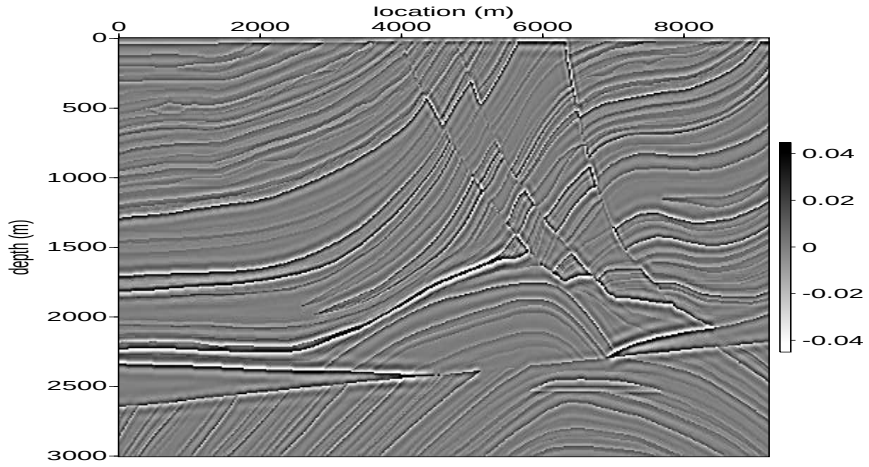

(b)

Figure 1: Smooth velocity model (a), reflectivity model (b) used to generate the synthetic born data.

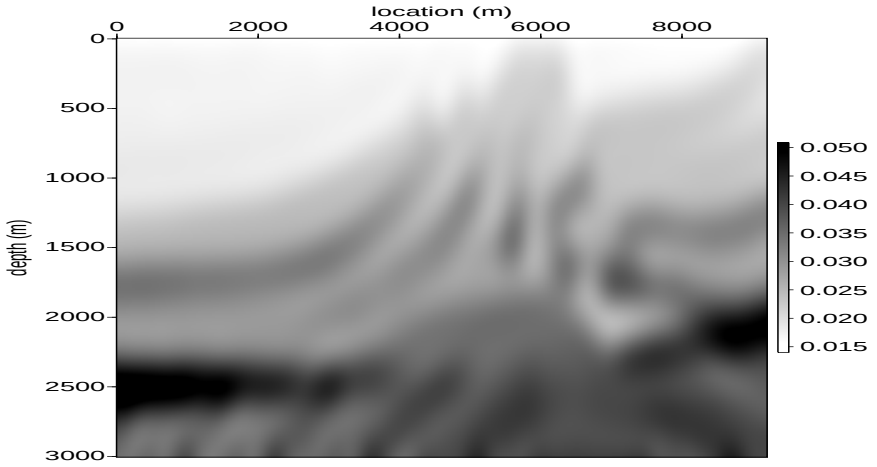

(a)

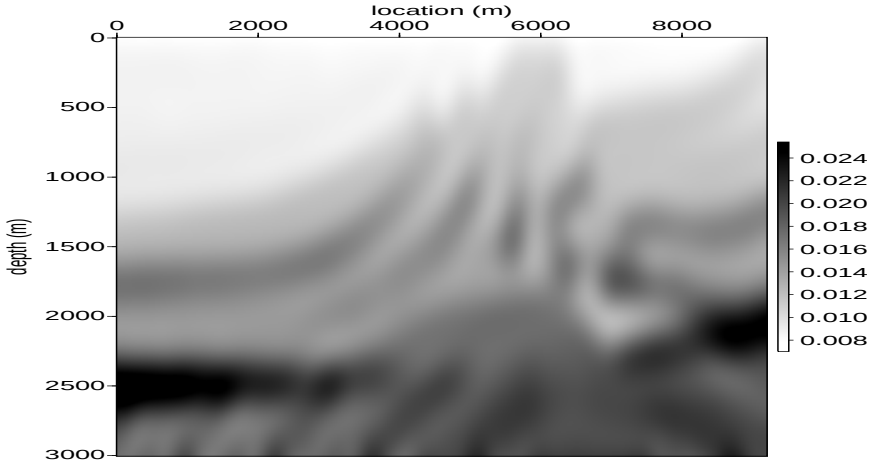

(b)

Figure 2: ϵ model (a) and δ model (b) used to generate the synthetic born data.

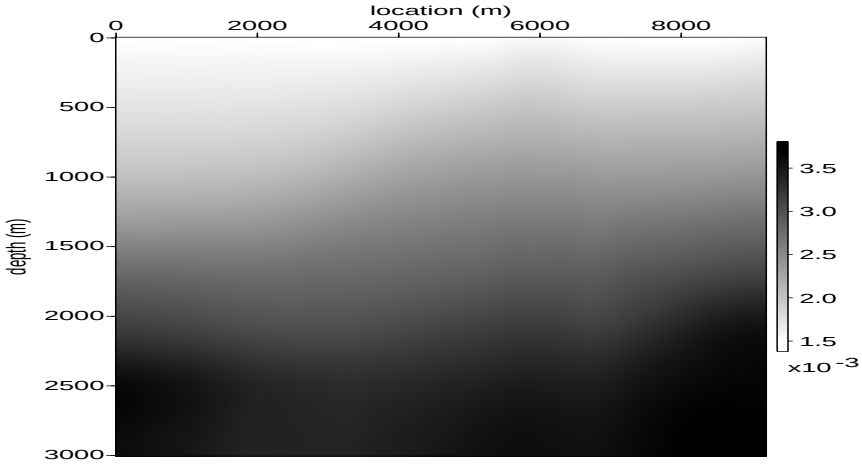

Figure 3: $\delta\epsilon$ model to test the objective function.

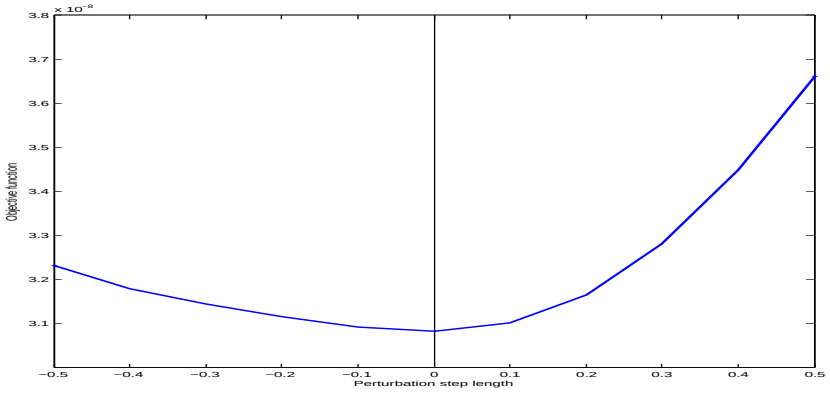

Figure 4: Objective function v.s. ϵ perturbation.

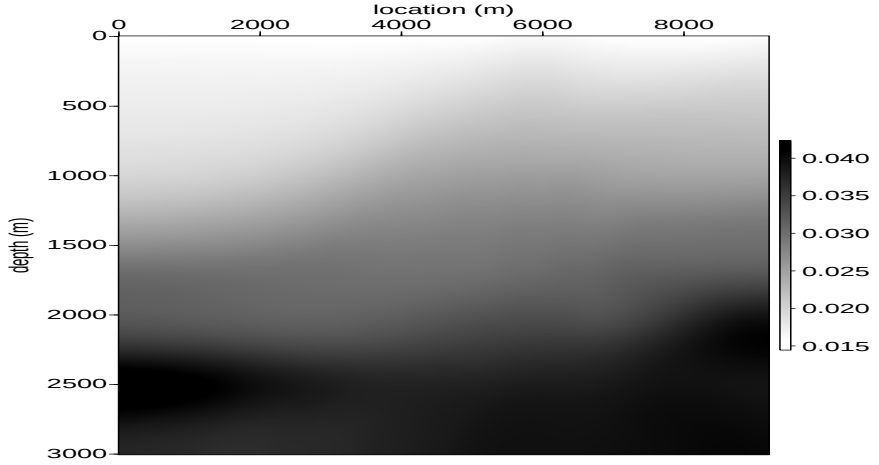

(a)

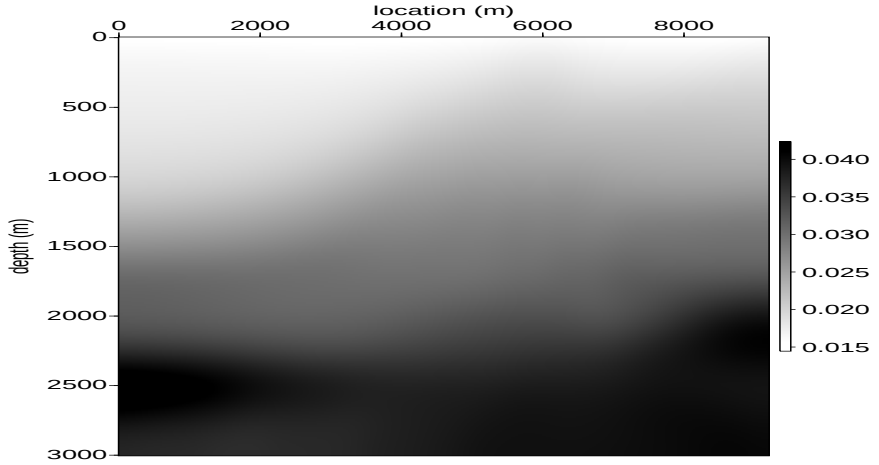

(b)

Figure 5: (a) True epsilon model; (b) True delta model to generate the synthetic data.

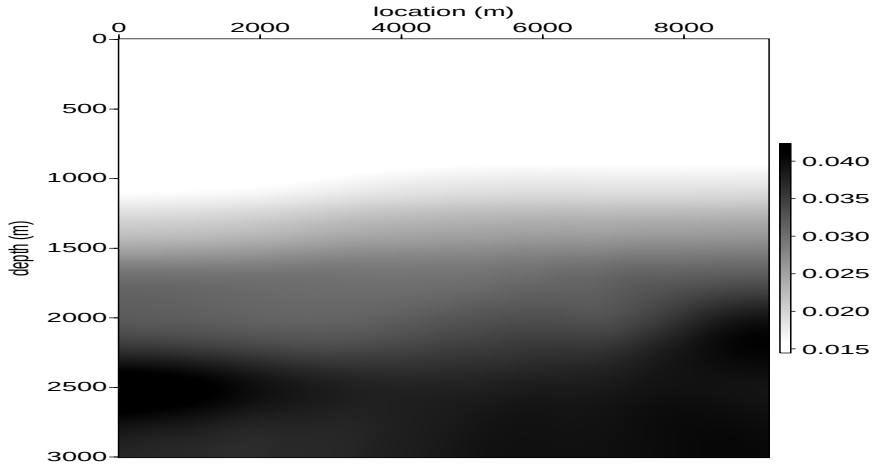

(a)

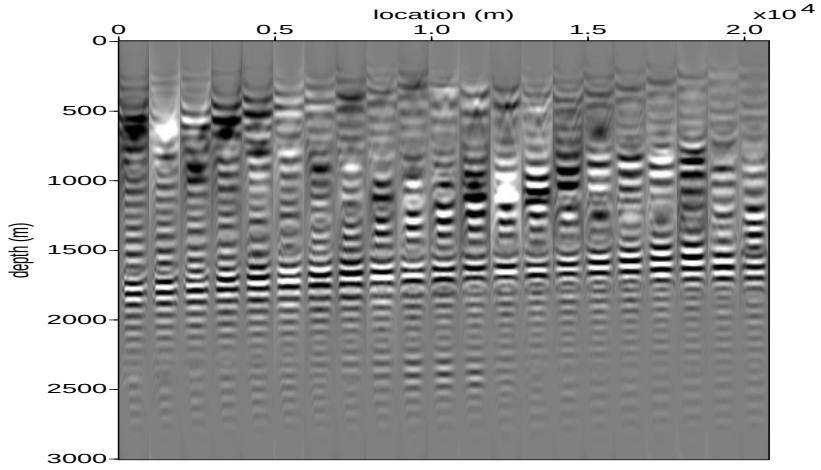

(b)

Figure 6: (a) Initial epsilon model; (b) Initial angle domain common image gathers using initial epsilon model.

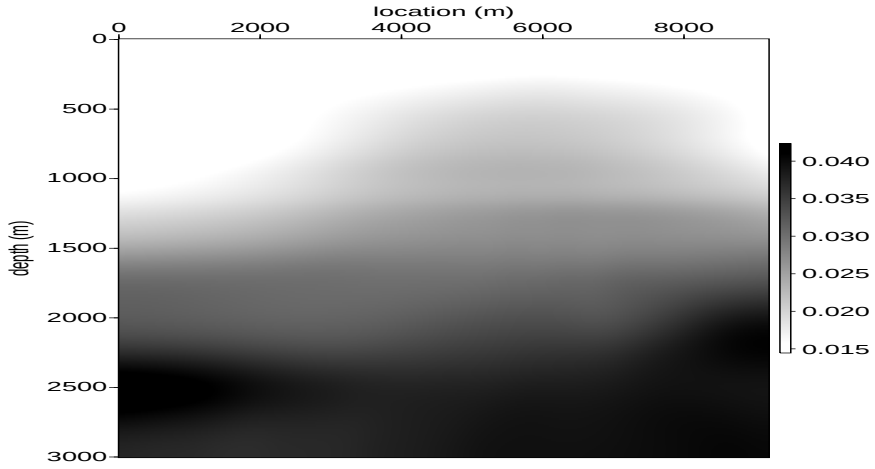

(a)

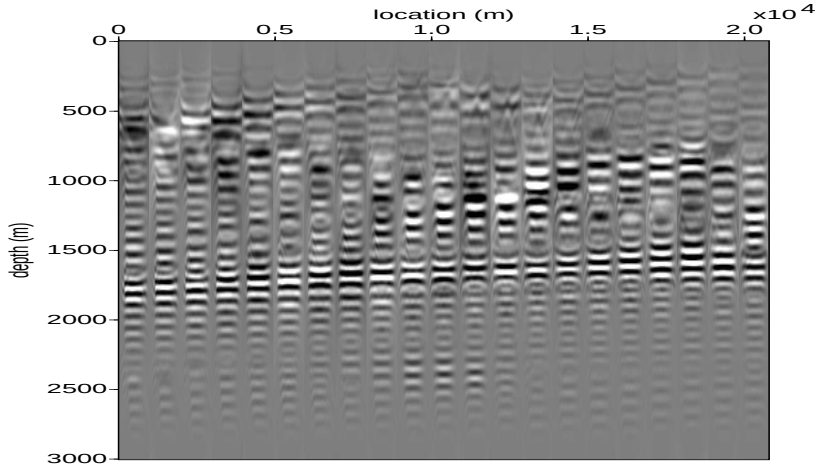

(b)

Figure 7: (a) Inverted epsilon model; (b) Final angle domain common image gathers using inverted epsilon model.

Joint inversion for two parameters

The tests in previous sections show that we have reliable objective function and successful inversion results for single parameter. However, joint inversion for more than one parameter for each grid in the subsurface is far more challenging due to the ambiguity between parameters. As a result, the preconditioning scheme using geological and rock physics information is crucial for its success.

In this test, we use the same synthetic data as last section. Unlike the last example where we use the perfect velocity model, the starting models for velocity and ϵ are both inaccurate. The initial velocity model and ϵ model are shown in Figure 8(a) and 6(a), respectively. The angle gathers generated using these initial models are shown in Figure 8(b). Significant moveout in the angle gather events indicates that the initial model is far from the true model. In fact, the initial velocity has a maximum of 15% error compared with the true velocity (Figure 1(a)) while the initial ϵ is 50% smaller than the true. Notice that error in velocity has a much larger effect on the kinematics of seismic wave, hence a larger effect on the flatness in angle domain.

After 40 iterations, we obtain the inverted velocity and ϵ model as shown in Figure 9(a) and 9(b). Comparing Figure 9(a) with Figure 1(a), we can conclude that the inversion has successfully recovered the high resolution vertical structure in the shallow part of the model. Due to the limited illumination, the steep structure in the deeper part of the model is not well resolved. Comparing Figure 7(a) and Figure 9(b), we notice that the inversion doesn't converge to the same solution due to the error in velocity. This is an indication that we haven't completely resolved the ambiguity between velocity and ϵ.

Angle gathers generated by the inverted model is shown in Figure 9(c). They are extracted from the same common image points as in Figure 8(b). The improved model flattens the gathers across the whole section. Notice that the low frequency energy in the water is the commonly seen wave-path energy for RTM images.

CONCLUSIONS

In this paper, we define an image-space inverse problem to solve for an optimized anisotropy model. To better describe the property of the subsurface and the wave propagation, we use the first-order VTI two-way wave equation to compute our Green's function. Test results on objective function show that flatness in angle domain is a valid measure of both velocity and anisotropic parameter ϵ. The results of single parameter and joint inversion demonstrate that we have successfully resolved the high frequency structure in velocity and successfully improved the anisotropic model where we have enough angle coverage. The updated image has flattened the gathers in the angle domain.

ACKNOWLEDGEMENT

We thank Shell International Exploration and Production Campany for permittion to publish this paper. Yunyue Li thanks the sponors of Stanford Exploration Project for their financial support.

REFERENCES

Bachrach, R., Y. K. Liu, M. Woodward, O. Zradrova, Y. Yang, and K. Osypov, 2011, Anisotropic velocity model building using rock physics: Comparison of compaction trends and check-shot-derived anisotropy in the gulf of mexico: SEG Expanded Abstract, **30**, 207–211.

Claerbout, J., 1987, Imaging the earth's interior: Blackwell Scientific Publications.

Claerbout, J. F., 2009, Image estimation by example.

Duveneck, E., P. Milcik, P. M. Bakker, and C. Perkins, 2008, Acoustic VTI wave equations and their application for anisotropic reverse-time migration: SEG Expanded Abstracts, **27**.

Fletcher, R., X. Du, and P. J. Fowler, 2009, Stabilizing acoustic reverse-time migration in TTI media: SEG Expanded Abstracts, **28**.

Guerra, C., Y. Tang, and B. Biondi, 2009, Wave-equation tomography using image-space phase-encoded data: SEP-report, **138**, 95.

Li, Y. and B. Biondi, 2011, Migration velocity analysis for anisotropic models: SEG Expanded Abstract, **30**, 201–206.

Li, Y., D. Nichols, K. Osypov, and R. Bachrach, 2011, Anisotropic tomography using rock physics contraints: 73^{rd} EAGE Conference & Exhibition.

McCollum, B. and F. Snell, 1932, Asymmetry of sound velocity in stratified formations: Physics (Journal of Applied Physics), **2**, 174–185.

Plessix, R.-E., 2006, A review of the adjoint-state method for computing the gradient of a funtional with geophysical applications: Geophys. J. Int., **167**, 495–503.

Sava, P. and B. Biondi, 2004a, Wave-equation migration velocity analysis-I: Theory: Geophysical Prospecting, **52**, 593–606.

———, 2004b, Wave-equation migration velocity analysis-II: Examples: Geophysical Prospecting, **52**, 607–623.

Sava, P. and S. Formel, 2006, Generalized imaging conditions for wave equation migration: CWP report, **524**.

Shen, P., 2004, Wave-equation Migration Velocity Analysis by Differential Semblance Optimization: PhD thesis, Rice University.

Shen, P. and W. W. Symes, 2008, Automatic velocity analysis via shot profile migration: Geophysics, **73**, VE49–VE59.

Tarantola, A., 1984, Inversion of seismic reflection data in the acoustic approximation: Geophysics, **49**, 1259–1266.

Woodward, M. J., 1992, Wave-equation tomography: Geophysics, **57**, 15–26.

Zhang, Y. and H. Zhang, 2009, A stable TTI reverse time migration and its implementation: SEG Expanded Abstracts, **28**.

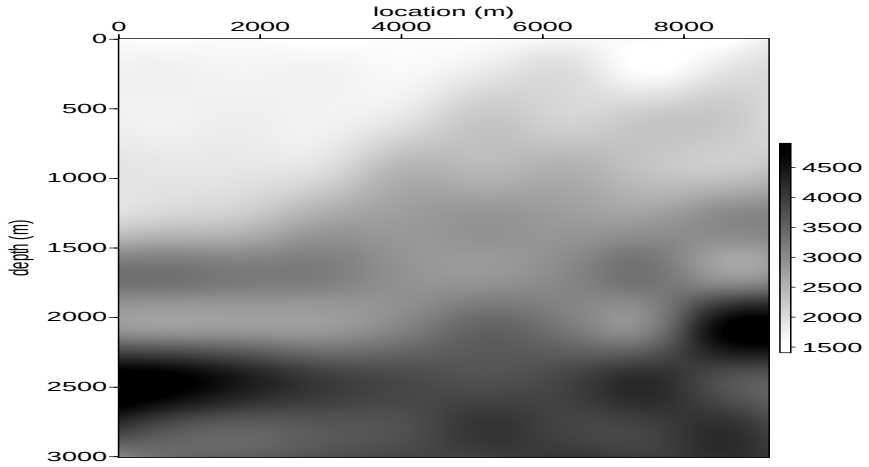

(a)

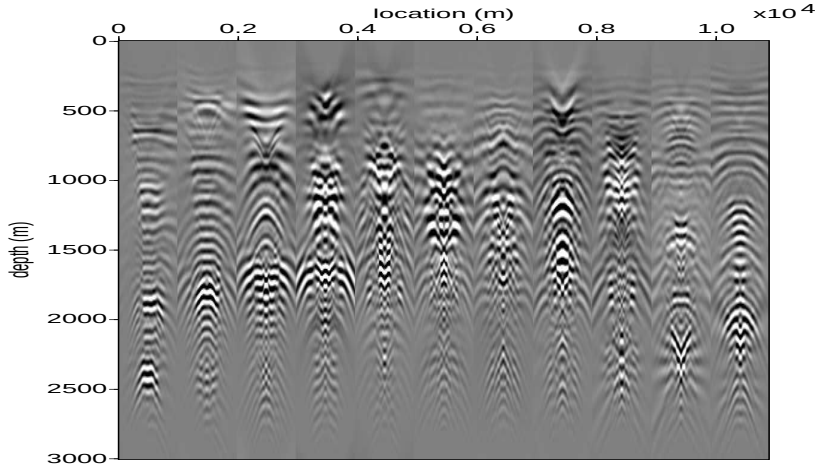

(b)

Figure 8: Initial velocity model (a) and the angle gathers (b) obtained by initial velocity model. Initial ϵ model is shown in Figure 6(a). Model error causes significant curvatures in the angle gathers.

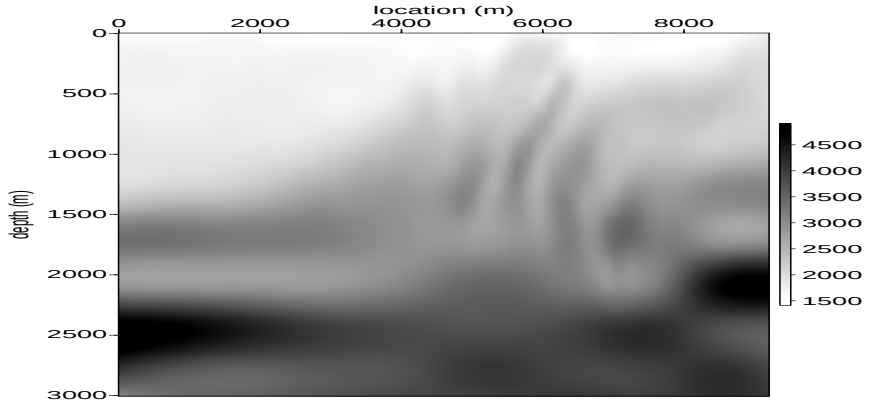

(a)

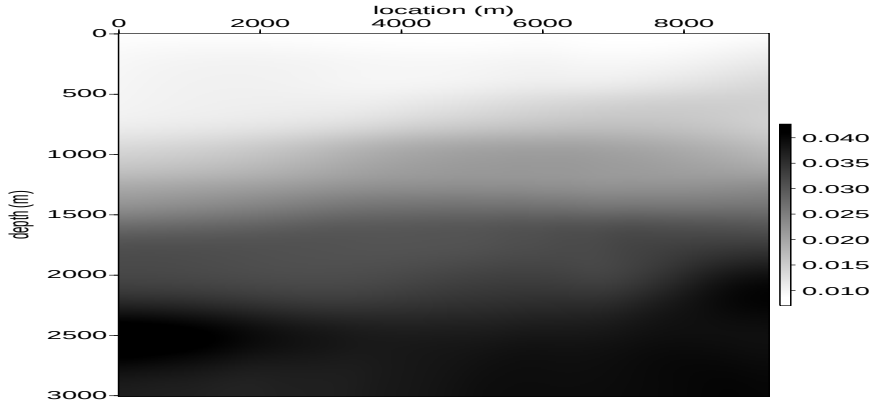

(b)

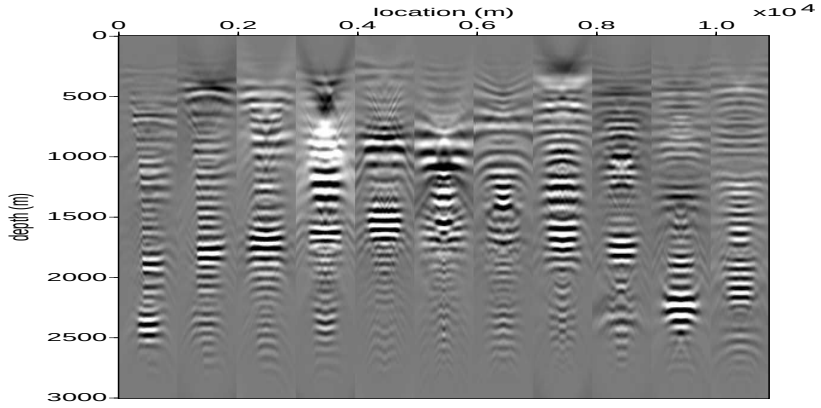

(c)

Figure 9: Inverted velocity model (a) and ϵ model (b) after 40 iterations. Angle gathers (c) obtained by the inverted model. Angle gathers are extracted at the same CIP as Figure 8(b). Improved velocity and ϵ flattens the corresponding angle gathers.